



BASIC SCIENCE ARTICLE

Optical coherence tomography for in vivo longitudinal monitoring of artificial dermal scaffold

Ziye Chen BE¹  | Qiong Cheng BM² | Lingyun Wang¹  | Yunfeng Mo BE¹ |
Ke Li MD² | Jianhua Mo PhD¹

¹Department of Electronic Information,
Engineering School of Electronics and
Information Engineering, Soochow University,
Suzhou, China

²Department of Burn and Plastic Surgery,
The First Affiliated Hospital of Soochow
University, Suzhou, China

Correspondence

Jianhua Mo, PhD, School of Electronics and
Information Engineering, Soochow University,
No. 1 Shizi St, 215006 Suzhou, China.
Email: joshuamo@gmail.com

Ke Li, MD, The First Affiliated Hospital of
Soochow University, No. 188 Shizi St, 215006
Suzhou, China.
Email: likefggf@163.com

Abstract

Objectives: Artificial dermal scaffold (ADS) has undergone rapid development and been increasingly used for treating skin wound in clinics due to its good biocompatibility, controllable degradation, and low risk of disease infection. To obtain good treatment efficacy, ADS needs to be monitored longitudinally during the treatment process. For example, scaffold-tissue fit, cell in-growth, vascular regeneration, and scaffold degradation are the key properties to be inspected. However, to date, there are no effective, real-time, and noninvasive techniques to meet the requirement of the scaffold monitoring above.

Materials and Methods: In this study, we propose to use optical coherence tomography (OCT) to monitor ADS in vivo through three-dimensional imaging. A swept source OCT system with a handheld probe was developed for in vivo skin imaging. Moreover, a cell in-growth, vascular regeneration, and scaffold degradation rate (IRDR) was defined with the volume reduction rate of the scaffold's collagen sponge layer. To measure the IRDR, a semiautomatic image segmentation algorithm was designed based on U-Net to segment the collagen sponge layer of the scaffold from OCT images.

Results: The results show that the scaffold-tissue fit can be clearly visualized under OCT imaging. The IRDR can be computed based on the volume of the segmented collagen sponge layer. It is observed that the IRDR appeared to a linear function of the time and in addition, the IRDR varied among different skin parts.

Conclusion: Overall, it can be concluded that OCT has a good potential to monitor ADS in vivo. This can help guide the clinicians to control the treatment with ADS to improve the therapy.

KEYWORDS

artificial dermal scaffold, image segmentation, longitudinal monitoring, optical coherence tomography

INTRODUCTION

Skin is the largest organ of the human body, which protects the underlying muscles, bones, ligaments, and organs. Serious skin damage can cause skin scar, dehydration, fatal infection, and death.¹ Skin loss is one of the common skin damages and to date, can be treated with surgical grafting methods, that is, skin grafts^{2,3} and flaps.^{4,5} For example, skin grafts can be used for treating traumatic wounds, defects after oncologic resection, congenital skin deficiencies, vitiligo,

and so on. Flaps are used preferentially for wounds with deep depth and bone exposed.⁶ However, although these living grafting methods contribute to the development of surgical grafting techniques, they still have some limitations.⁷ Specifically, these two methods are not well suited for large skin wounds and may take a risk of stimulating the trauma.^{1,8} The limitations above prompted the development of tissue engineering technology for producing bioengineered equivalents-dermal scaffold, which can be applied in clinical treatment for skin wounds. Till now, the dermal scaffold has been utilized for treating

Ziye Chen and Qiong Cheng are co-first authors and contributed equally to this study.

various skin wounds, such as full-thickness wounds,⁹ postoperative ulcers,¹⁰ burns contractures,¹¹ and pressure sores.¹² Compared with conventional autologous skin grafting, the dermal scaffold can effectively improve the cosmetics features of wound recovery, improve the recovery speed, avoid additional trauma caused by autologous skin harvesting, and reduce the risk of infection.^{13,14}

The dermal scaffold can be classified into the natural dermal scaffold and artificial dermal scaffold (ADS).¹⁵ Natural dermal scaffold is produced from allogeneic or heterologous skin by removing epidermal and dermal cells while preserving extracellular dermal matrix.¹⁶ It shows the advantages of high survival rate, soft texture, and light scarring. However, it suffers from limited sources, high cost, and high biorisk.^{17,18} In contrast, ADS is produced from natural materials (i.e., collagen,¹⁹ elastin,²⁰ and alginate²¹) and synthetic materials (polyethylene glycol,²² poly(vinyl alcohol)²³ and polycaprolactone²⁴). It exhibits the advantages of good biocompatibility, controllable degradation, and low risk of disease infection.^{18,25} Till now, collagen-based ADS has been commercialized and widely used in clinics.^{25–28} It has been well accepted that dermal scaffold degradation, cell in-growth, vascular regeneration, and scaffold-tissue fit are the key structural properties to be monitored. ADS provides a suitable substrate for cell growth and vessel regeneration²⁹ and thus the rate of the cell in-growth and vessel regeneration is critical for the clinicians to determine the timing of the second-stage skin transplantation.³⁰ The degradation rate also plays a key role in cell adhesion, proliferation and penetration in wound recovery³¹ and consequently needs to be under control.³² As for the scaffold-tissue fit, there often exist air gaps between the scaffold and the tissue, which may slow down the vascularization of the scaffold and consequently needs to be eliminated.³³

In comparison to the continuously growing use of ADS, the supporting evaluation techniques are behind-hand. Currently, the cell in-growth, vascular regeneration, and scaffold degradation are often evaluated in vitro through imaging the excised tissues under a microscope which are stained with hematoxylin-eosin or Masson's trichrome.³⁴ However, these methods require harvesting specimens from the dermal scaffolds, which is invasive and painful.^{34,35} The scaffold-tissue fit is usually evaluated by visual observation of the scaffold's surface appearance, which is highly dependent on the clinician's experience and consequently subjective. Therefore, in vivo imaging techniques are desired to delineate the dermal scaffold to obtain an accurate measurement on the cell in-growth, vascular regeneration, and scaffold degradation as well as the detection of the scaffold-tissue gap. Several conventional clinical imaging techniques have been used for monitoring the wound healing process based on the dermal scaffold. For example, high-resolution ultrasound has been applied to

assess the structural changes deep in the wound.³⁶ Magnetic resonance imaging has been employed to evaluate the fit of human decellularized dermal matrix with the surrounding tissues.³⁷ However, these two imaging techniques cannot differentiate the micro-structural changes due to the limited resolution.³⁸ In 2016, Fox et al proposed to incorporate fluorescent nanodiamond into the scaffold, allowing for assessing the scaffold degradation by fluorescence imaging.³⁹ However, it is invasive due to the use of imaging contrast agent and incapable of detecting the air gap between the scaffold and the tissue.

Optical coherence tomography (OCT) can provide three-dimensional images of weak-scattering biological tissues with a resolution at micrometers by utilizing low-coherence optical interference.⁴⁰ OCT has achieved a great success in ophthalmology in the past decades and has become a clinical routine in ophthalmology.^{41–43} Besides, dermatology is another medical field where OCT has undergone great advances from both the technical aspect and the clinical application aspect.^{44–46} Specifically in clinical applications, OCT can be used to observe the structure changes associated with various skin diseases.⁴⁷ For example, OCT has been used for the detection of nonmelanoma skin cancer^{48,49} and inflammatory dermatoses, that is, psoriasis and eczema.⁵⁰ In particular for skin wound, OCT has been developed to assess the wound depth,³⁸ wound healing,^{51–53} and detect subcutaneous parasites.⁵⁴ In addition, OCT can also be utilized for inspecting skin equivalent used in wound healing, including the structure and thickness.^{38,55–57} However, skin equivalent evaluation with OCT is limited to in vitro study. To the best of our knowledge, OCT has not yet been employed to monitor the wound healing process with ADS in vivo and measure the ADS degradation and the tissue growth on human skin.

In this work, we propose to utilize OCT to monitor the tissue growth and the ADS degradation and the scaffold-tissue fit. A clinic OCT prototype with a handheld probe is developed for in vivo skin imaging and a semiautomatic segmentation algorithm is designed based on U-Net to segment the ADS for quantitative analysis. Our method is evaluated on three patients treated with ADS. Good quality three-dimensional images of the dermal scaffold can be acquired for evaluating the ADS degradation and tissue growth. The results demonstrate the great potential of OCT for in vivo monitoring of wound treatment with ADS.

METHODS

Patients

A total of three patients were recruited at the department of burn and plastic surgery of the First Affiliated Hospital of Soochow University, including two males

and one female, who are 23–64 years old as described in Table 1. The wounds are located at the ankle, head, and instep, exhibiting a size of $1.5\text{ cm} \times 1.2\text{ cm}$ to $10\text{ cm} \times 8\text{ cm}$. All the wounds are treated with artificial dermal scaffold (BAS-1208, Lando). The ADS is constructed with silicon film layer (SFL, thickness: $0.25 \pm 0.15\text{ mm}$) seated on top of collagen sponge layer (CSL, thickness: $0.25 \pm 0.15\text{ mm}$). Approximately in 2 weeks after applying the ADS, a second-stage free skin graft (Split-thickness skin graft, thickness: $0.25 \pm 0.05\text{ mm}$) is used to replace the SFL, which is aimed to reduce the chance of infection and improve the esthetics of the wound.⁵⁸ The study was approved by the Human Research Ethics Committee of the First Affiliated Hospital of Soochow University, and the research was conducted with the principles embodied in the Declaration of Helsinki and in accordance with local statutory requirements.

OCT prototype system

A clinical OCT system with a handheld probe was developed for in vivo OCT imaging on human skin as depicted in Figure 1A. The OCT system is designed based on Mach-Zehnder interferometer with a wavelength-swept light source. The light source's output (SS-OCT1060, Axsun Technology) sweeps from about 1000–1100 nm at a rate of 100 kHz. The sample arm consists of a collimator (F280APC-1064, Thorlabs), a pair of galvo-scanners (GVSM002/M, Thorlabs), and a focusing lens (AC254-060-B, Thorlabs), which are built into a compact case to

create a handheld probe. The probe tip is armed with an imaging window (WG10530-B, Thorlabs) tilted at an angle of 10° to reduce the specular reflection on the skin surface. The reference arm is built based on a one-way light path with a pair of collimators (F240APC-1064, Thorlabs). The reference signal and the sample signal are combined with a 50/50 fiber coupler and eventually fed into a balanced detector (PDB471C, Thorlabs). The balanced detector's output passes through a low-pass filter (SLP-150+, Mini-circuits) to block the signal with a frequency higher than 155 MHz and then is recorded in a computer via a 12-bit dual-channel data acquisition card (ATS9351, Alazartech). The light beam scanning is realized by using a pair of galvo-scanners driven by a 16-bit high-speed analog output device (PCIE-6363, National Instruments). The axial resolution and lateral resolution of the OCT system are about $10.7\text{ }\mu\text{m}$ (in air) and $20\text{ }\mu\text{m}$, respectively, and the imaging depth in air is about 3.78 mm. A clinic-friendly software is developed with a user-interface to show B-scan in real-time.

Imaging protocol

OCT imaging is carried out on each patient from the application of the ADS to the second-stage skin transplantation until the complete uptake of the scaffold. Three to seven OCT scans are acquired from different parts of the wounds depending on the wound size upon the patients' visit to the clinicians. Each OCT imaging (C-scan) covers a field of $2.8\text{ mm} \times 2.8\text{ mm}$ (512×512 pixels). The corresponding A-scan consists of 672 pixels. With an A-scan rate of 100 kHz, each C-scan takes about 3 s.

TABLE 1 Patient information.

Patient	Age	Gender	Wound Area
1	58	Male	Ankle
2	23	Female	Head
3	64	Male	Instep

IRDR quantification

In this study, a cell in-growth, vascular regeneration, and scaffold degradation rate (IRDR) is defined as the volume reduction rate of the scaffold's collagen sponge layer as the cell in-growth, vascular regeneration, and scaffold

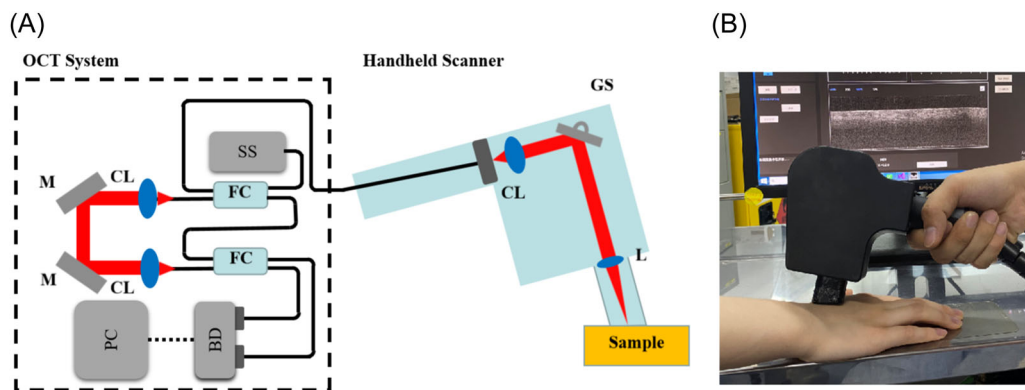


FIGURE 1 (A) Schematic of the clinical OCT system, (B) Photograph of the handheld OCT probe. BD, balanced photodetector; CL, collimator; FC, fiber coupler; GS, galvo scanner; L, lens; M, mirror; PC, personal computer; SS, swept source.

degradation are the main causes of the volume reduction of the scaffold's CSL layer which are measurable in OCT image. In detail, the cell grows and the vessel regenerates into the CSL from the bottom, and concomitantly the CSL undergoes an uptake (degradation). The CSL part occupied by the regenerated tissue will appear to be different from the CSL part with no or much less regenerated tissue in OCT image. Thus, it is reasonable to measure the IRDR to assess the extent of the tissue regeneration and scaffold degradation. The IRDR ($V_{IRDR}^{\%}$) is calculated by using the formula: $V_{IRDR}^{\%} = (V_0 - V_1)/V_0 \times 100$ (%), where V_0 and V_1 denote the volumes of the CSL layer measured at two different time points. The volume can be measured based on the 3D image of the scaffold produced by OCT.

Dermal scaffold segmentation

To determine the IRDR based on the volume as discussed above, the CSL of the dermal scaffold needs to be segmented from the OCT image. Hence, a semi-automatic segmentation algorithm is designed based on U-Net network for extracting the CSL from OCT images. The segmentation can be divided into two steps as the following.

First, a U-Net network model is built for segmentation as shown in Figure 2. The segmentation is implemented on B-scans as U-Net has been well demonstrated in two-dimensional medical image segmentation.^{59,60} The segmented B-scans are fused to form a 3D image of the dermal scaffold. In total, there are 30 3D image data sets, of which each consists of 512 B-scans. Eighteen B-scans from each 3D image which are evenly

distributed along C-scan are chosen for training and testing the segmentation model. Consequently, there are totally 540 images, of which 70% (378 images) are selected for training and the remaining 30% (162 images) are for testing. The ground truth is obtained by manual labeling under the guidance of experienced clinicians.

Next, a boundary fitting algorithm is implemented to improve the segmentation to increase the measurement accuracy of the dermal scaffold's volume. This fitting algorithm is developed with the assumption that the scaffold structure shows a rigorous continuity and the dermal scaffold's boundary alters by less than one pixel between the consecutive B-scans. The fitting process works as following: (1) the CSL of the dermal scaffold in the first B-scan of a 3D OCT image is annotated manually as the starting reference image; (2) the CSL's boundary in the neighboring B-scan is compared to that in the reference image. If the boundary is N pixels ($N > 1$) away from the reference, it will be pulled towards the reference by $N - 1$ pixels as illustrated in Figure 3. Otherwise, the boundary will remain unchanged. For example, pixel P1 is pulled downwards the green pixel by one pixel while pixels P2–P7 remain stationary; (3) the newly adjusted boundary is set as the reference for next B-scan; (4) the second and third procedures above are repeated until all the B-scans are adjusted.

RESULTS

In this study, we investigated the feasibility of using OCT to monitor ADS longitudinally from two aspects: the scaffold-tissue fit and the IRDR.

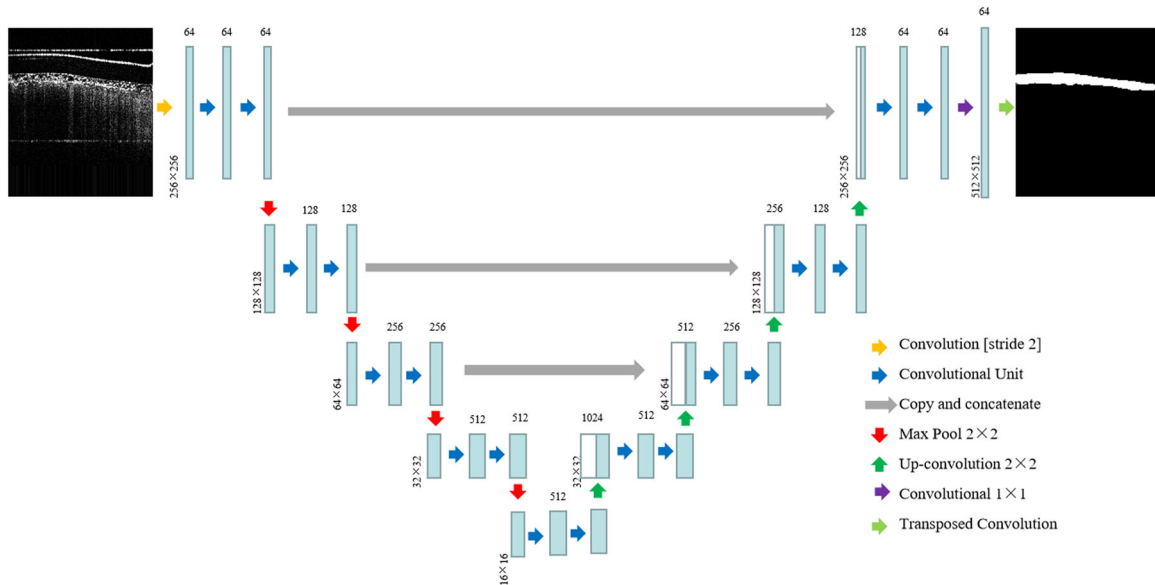


FIGURE 2 Neural network architecture of the U-net network model. Light blue box refers to a three-dimensional tensor. The number on top of each box denotes the number of channels (the number of filters). The number at the lower left side of the box provide the x - y -size. White boxes in the decoder part represent the concatenated tensor correspondents in the encoder part. The arrows denote the different operations.

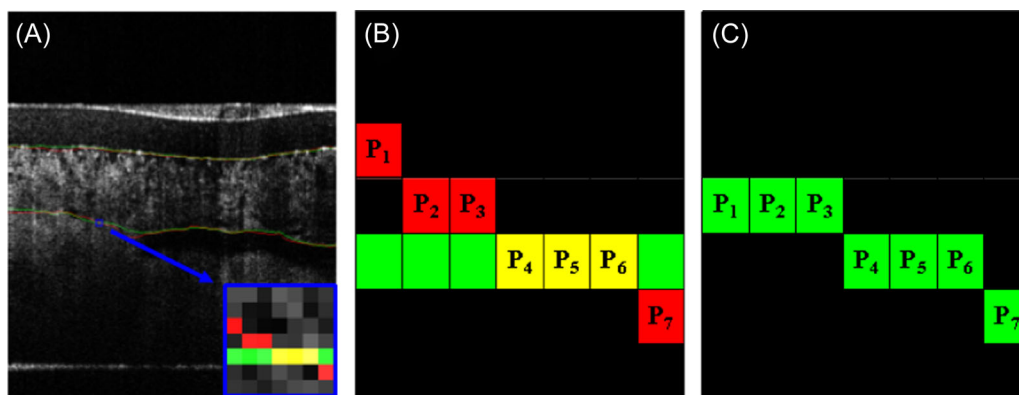


FIGURE 3 (A) B-scan of a dermal scaffold, (B) Zoomed-in image from (A), (C) New boundary yielded by the fitting process. In (A) red and green lines represent the boundaries of the collagen sponge layer obtained by U-Net segmentation and of the reference image, respectively, and yellow lines delineate the overlap between the red and green lines.

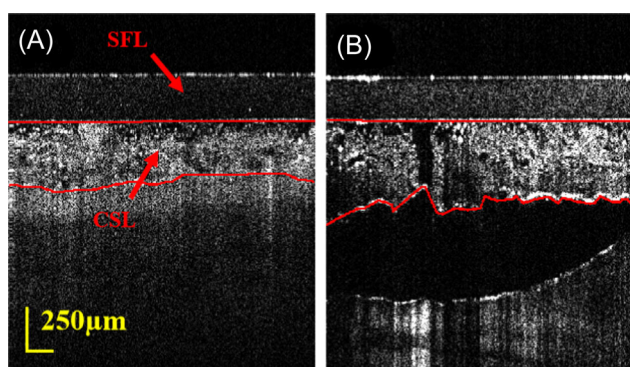


FIGURE 4 B-scan of a dermal scaffold: (A) Good scaffold-tissue fit and (B) poor scaffold-tissue fit. The red curve delineates the upper and lower boundaries of the collagen sponge layer.

Dermal scaffold fit

OCT imaging can provide a good insight into the structure of the dermal scaffold as illustrated in Figure 4. It is clearly seen that the dermal scaffold consists of two layers which are SFL on the top and CSL on the bottom. The SFL appears to be transparent which can be attributed to the low scattering capability. In comparison, the CSL shows a higher intensity and a sponge-like structure which is significantly different from the underlying skin. This allows for discriminating the CSL from the skin, paving the way for identifying the air gap between the CSL and the skin. Figure 4B describes an example of a loose fit of CSL with the underlying skin tissue. The CSL is largely detached from the skin.

IRDR of dermal scaffolds

OCT can determine the IRDR of the dermal scaffold by quantifying the CSL's volume alteration since the CSL can be clearly imaged by OCT. Figure 5A shows a

wound covered with ADS which is due to skin ulcer on the ankle associated with diabetes. The wound underwent OCT imaging at 2-, 6-, and 9-days after applying the dermal scaffold. Figure 5B–D give the B-scans for those three-time slots, respectively. It is seen that the CSL delineated with red boundaries exhibits a clear trend of thinning associated with the cell in-growth, the vessel regeneration, and the ADS degradation while the SFL does not show any significant thickness change. Figure 5E depicts the cross-sectional image of the dermal scaffold at 5-days after the second-stage free skin transplantation which was done 2 weeks after the dermal scaffold was applied to the wound. The second-stage free skin transplantation replaced the SFL with free skin. As a result, there is no transparent layer on top of the CSL and instead is a bright scattering layer which is the free skin. Moreover, the CSL becomes much thinner as compared to that before the second transplantation, indicating continuous degradation and tissue growth. In addition, it is also observed that the CSL's up boundary appears to be wrinkled due to the compression by the free skin as compared to the image before the second transplantation.

Besides, more morphological alterations can be found in the en-face images (Figure 5F–I). At the early stage of the dermal scaffold application, the en-face image exhibits a uniform scattering structure at the depth near the SFL layer (Figure 5F). In comparison, the structure tends to lose its uniformity over time as shown in Figures 5G–H. Both the amount of holes and the hole's size increase from Figure 5F–H. As for Figure 5I, the CSL is referred to as the dark area while the bright area represents the skin tissue, implying that the CSL nearly undergoes a complete cell in-growth and vessel regeneration.

To measure the CSL's volume for determining the IRDR, CSL segmentation is required. Four prevailing deep learning networks, including U-Net,⁶¹ U-Net++,⁶² Attention U-Net,⁶³ and CS-Net,⁶⁴ were evaluated in the

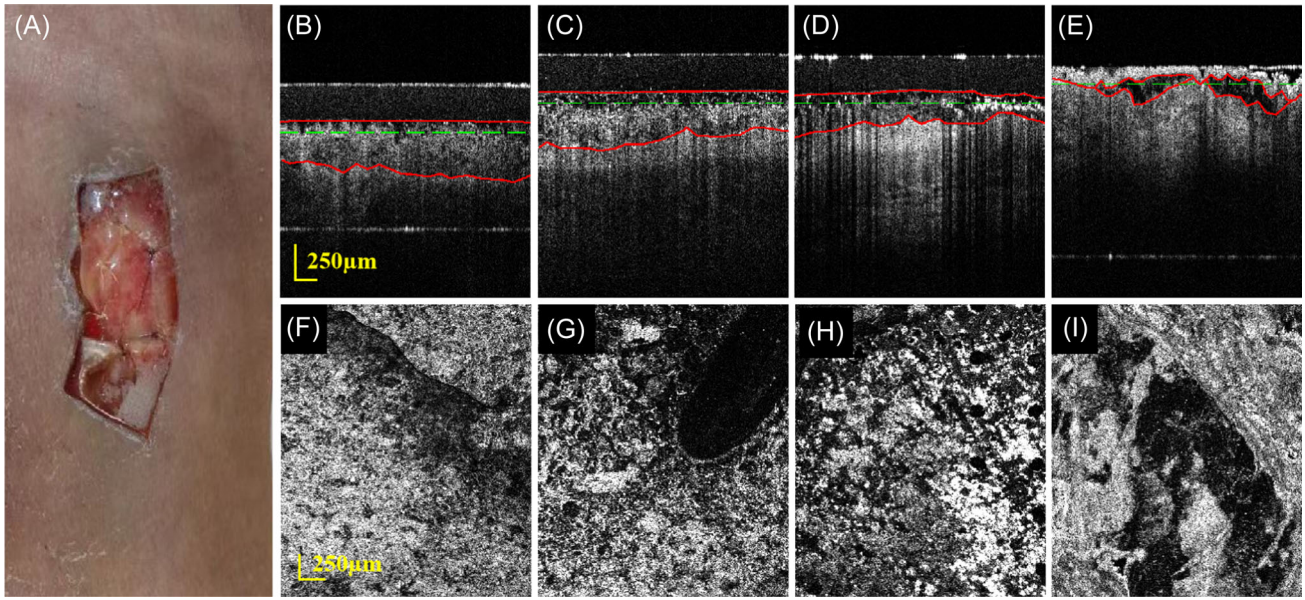


FIGURE 5 (A) Photo of patient's wound covered with a ADS, (B)–(D) B-scan of the ADS at 2-, 6-, and 9-days after dermal scaffold coverage, respectively, (E) B-scan of the ADS at 19-days after dermal scaffold coverage and 5 days after second-stage skin transplantation, (F)–(I) are the en-face images of the CSL corresponding to (B)–(E). The green dashed line in (B)–(E) indicates the depth of the en-face image, and the red curve is the upper and lower boundaries of the CSL. CSL, collagen sponge layer.

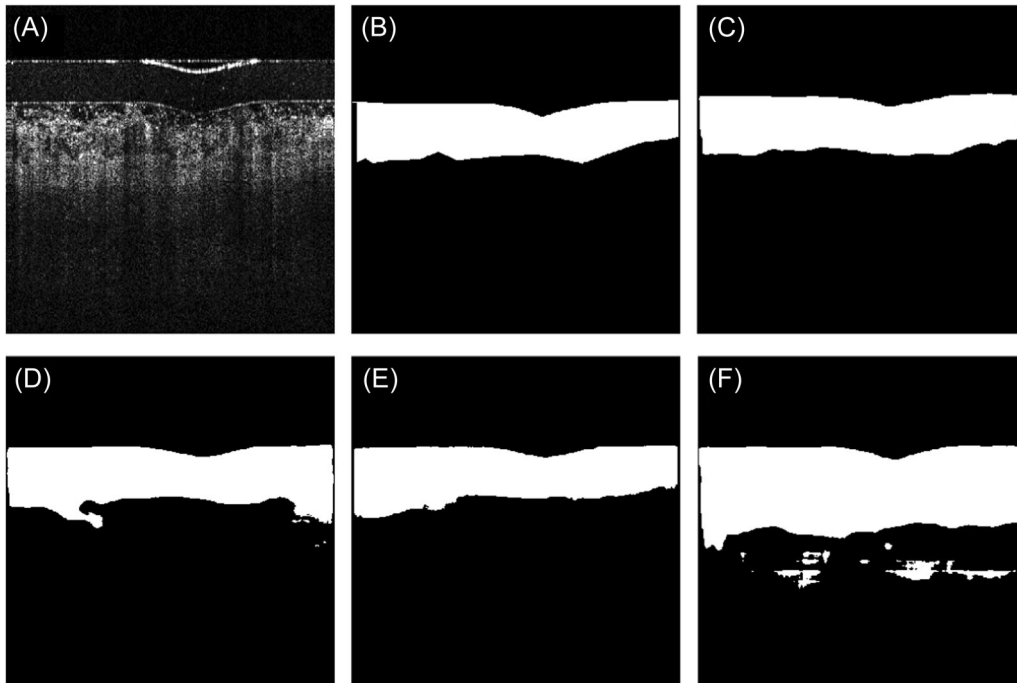


FIGURE 6 (A) B-scan of the ADS, (B) manual segmentation results, (C)–(F) are the collagen sponge layer segmented by U-Net, U-Net++, Attention U-Net, and CS-Net, respectively.

CSL segmentation. Figure 6 describes an example of CSL segmentation by those four networks above. The segmentation by U-Net shows an optimal match with the ground truth. The segmentation was evaluated with five metrics, including Pre, Recall, IoU, Dice, and F-score⁶⁵ which are summarized in Table 2. It is clearly seen that

overall, U-Net performs the best among those four networks with the highest Recall (0.7474), IoU (0.6537), Dice (0.7762), and F-score (0.8112). Consequently, the following process and analysis are conducted based on the CSL images segmented with U-Net. To reduce the impact of the segmentation on the CSL volume

measurement, a boundary-fitting algorithm was developed to correct those segmentation errors by utilizing the structural continuity between consecutive B-scans. It is found that the Pre, Recall, IoU, Dice, and F-score are increased by the fitting algorithm from 0.8871, 0.7474, 0.6537, 0.7762, and 0.8112 to 0.8882, 0.9036, 0.8032, 0.8873, and 0.8958, respectively.

Figure 7A–D show the segmented 3D images of the CSL corresponding to Figure 5B–E, respectively. Based on the 3D images, the thickness maps are computed as illustrated in Figure 7E–H. The thickness seems not to be uniform and as seen in Figure 7A, the thickness varies a lot laterally. However, a clear thinning trend can be found over time. In addition, after the second-stage free skin transplantation (Figure 7D), the CSL shows a big loss.

Next, the segmented CSL image is binarized with the noise floor as the threshold. The noise floor is determined by averaging the intensity over the holes in the CSL image. With the binary image, the CSL volume is measured by counting all the nonzero pixels. Figure 8 depicts the CSL IRDR of three patients as a function of time. For each degradation calculation, the volumes of

two to three good-quality 3D images are averaged, which are acquired at various positions of the same wound. It needs to be pointed out that two 3D images are excluded due to their significantly larger CSL volumes as compared to other 3D images measured on the same day. For one 3D image, the large CSL volume is probably due to the large detachment of ADS from the underlying tissue. This detachment can prevent protease from infiltrating the scaffold and consequently slow down CSL degradation. For the other 3D image, it may

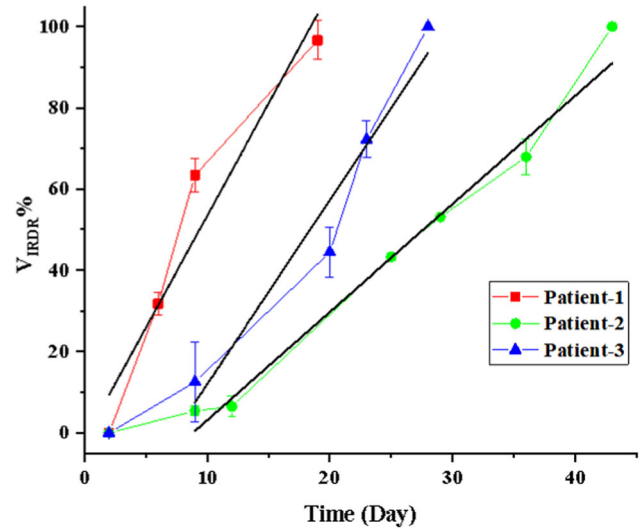


FIGURE 8 The IRDR of the collagen sponge layer as a function time. The black line represents the linear fitting of the IRDR function. Error bars are standard deviation.

TABLE 2 CSL segmentation results.

Methods	Pre	Recall	IoU	Dice	F-score
U-Net	0.8871	0.7474	0.6537	0.7762	0.8112
U-Net++	0.9308	0.6903	0.6455	0.7666	0.7927
Attention U-Net	0.8920	0.6919	0.6194	0.7466	0.7793
CS-Net	0.9524	0.6107	0.5902	0.7165	0.7442

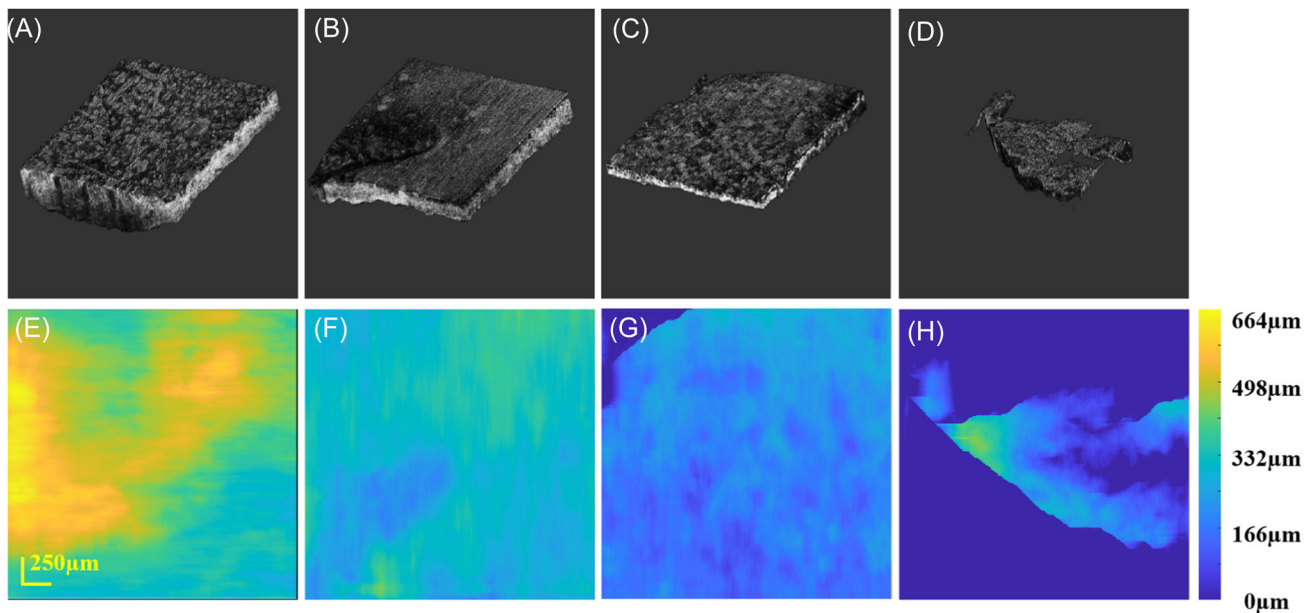


FIGURE 7 (A)–(D) Three-dimensional images of the segmented CSL corresponding to Figure 5B–E, respectively. (E)–(H) Thickness maps measured from (A)–(D), respectively.

be explained by the segmentation error due to the weak distinction between the CSL and the tissue.

For each patient, the first 3D image is used as the base (undegraded) for the IRDR calculation and consequently the corresponding IRDR is zero. Overall, similar IRDRs are observed on patients 1 and 3 while much slower IRDR on patient 2. In addition, for patients 2 and 3, the dermal scaffold undergoes a slow IRDR during the first 9 days followed by a fast IRDR. This trend does not occur on patient 1. This may be because the wounds on patients 2 and 3 are treated with a negative pressure drainage system for 1 week after the dermal scaffold is applied. To evaluate the IRDR trend quantitatively, the IRDR curves are fitted with a linear function to obtain an average IRDR. Due to the impact of the negative pressure drainage system, the starting IRDR is excluded in the fitting process for patients 2 and 3 to achieve a fair comparison among all three patients. The slopes of the linearly fitting function are 5.51, 2.66, and 4.53 percentage/day for patients 1–3, respectively.

DISCUSSION

In this study, we demonstrated that OCT imaging is well capable of visualizing the fit of the dermal scaffold with the neighboring natural tissue as illustrated in Figure 4. This can effectively help clinicians to find and locate the loose fit, and take measures, that is, compression, to obtain a tight fit. If the loose fit is untreated, this will

obscure the vascularization of the CSL. This can be accounted for by the fact that the detachment prevents the extracellular matrix secretion from impregnating the scaffold, and the fibroblasts from growing into the dermal scaffold, and results in reduced delivery of nutrient into the dermal scaffold.⁵⁸ Furthermore, the survival rate of the free skin tissue is greatly dependent on the degree of the CSL's vascularization. Consequently, a tight dermal scaffold fit is highly desired to achieve a high survival rate of the transplanted skin.^{33,66}

As for the IRDR measurement, the ADS underwent an IRDR increase at a similar speed for patients 1 and 3. This may be explained by the fact that both wounds are on the ankle. In addition, these two patients show the same sex and a similar age. In comparison, the IRDR increase's speed was reduced nearly by a fact of two for the dermal scaffold applied to the head. These findings imply that the IRDR is likely to be dependent on the wound location and a consistent IRDR can be expected for the same skin location. However, a larger data set is needed to further verify it.

Finally, it is worth taking out patient 3's last OCT imaging results for further analysis which was obtained at 13 days after the second-stage skin transplantation. The wound is a skin ulcer caused by scalding as shown in Figure 9A. The patient recovered well after skin transplantation and did not suffer any inflammation. In B-scan (Figure 9B), it seems that there is no CSL left inside the tissue, indicating that the CSL has been completely filled with newly grown cells and blood

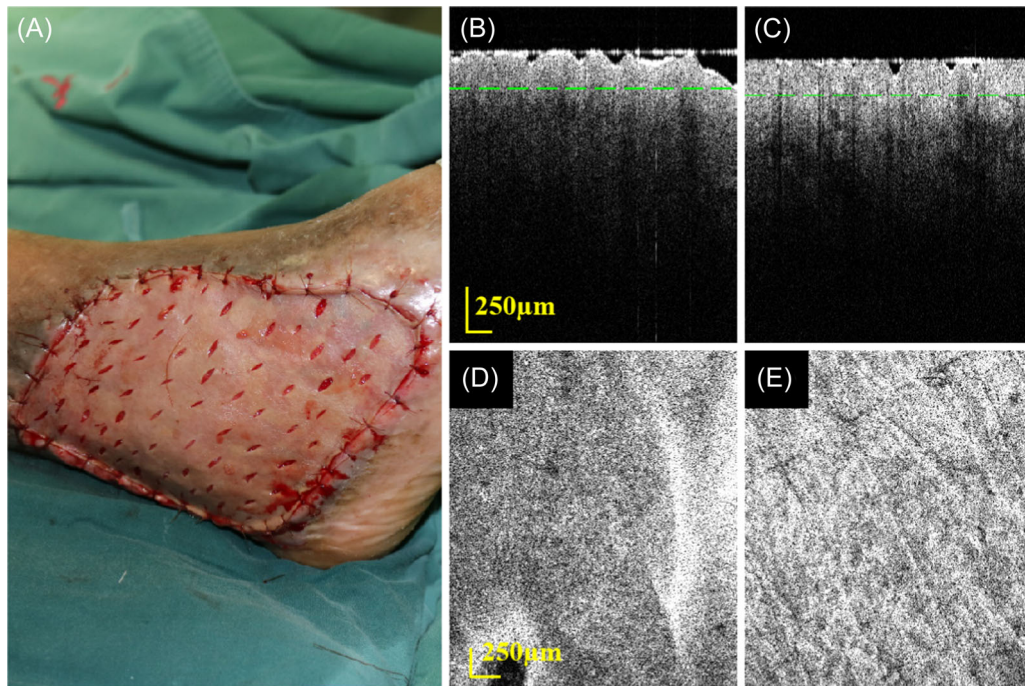


FIGURE 9 (A) Photo of patient's wound covered with free skin, (B) and (C) B-scans of the wound at 13-days after free skin transplantation and healthy skin, respectively, (D) and (E) en-face images of the collagen sponge layer corresponding to (B) and (C). The green dashed line in (B)–(C) denotes the depth of the en-face image.

vessels, and most of the CSL has degraded. The IRDR at 5 days earlier is measured to be about 70%. According to the IRDR function, this complete disappearance of CSL should be close to the last OCT measurement. Moreover, this dermal scaffold treatment can be assessed by comparing with the surrounding healthy tissue. In the B-scans of the treated tissue and the healthy tissue (Figure 9B,C), it is seen that the blood vessels start to be present around the depth denoted with green dashed line and more large vessels are observed in the healthy tissue, which are more obvious in the corresponding en-face images (Figure 9D–E). This suggests that OCT angiography can further enhance the capability of OCT in evaluating wound treatment with ADS by providing vasculature images.

CONCLUSION

In this work, OCT was proposed to monitor the ADS in vivo. An OCT prototype with a handheld probe was developed for clinical measurement. It is demonstrated successfully that OCT imaging can provide a rapid and accurate evaluation about the fit of the dermal scaffold with the natural skin tissue. Moreover, OCT imaging was utilized for evaluating the dermal scaffold's degradation, cell in-growth and vascular regeneration by measuring the IRDR. The IRDR was determined based on the scaffold volume and thus, a semi-automatic image segmentation model based on U-Net was designed to segment the CSL from OCT image for the volume measurement and furthermore a boundary fitting algorithm was developed to improve the volume measurement by reducing the impact of the segmentation errors. The results show that OCT imaging has a good potential to be an effective tool for longitudinally monitoring the dermal scaffold's IRDR in vivo. This can help clinicians to make the dermal scaffold degrade and the tissue grow at a proper rate to obtain good wound therapy efficacy. In the future, the method developed for measuring the IRDR will be validated on a larger data set from various skin parts of human body and further optimized to be used as a clinical routine. In addition, OCT angiography will be integrated into the current method to provide a more extensive evaluation.

ACKNOWLEDGMENTS

This study was supported by the National Natural Science Foundation of China, Grant Number: 81401451 and Natural Science Foundation of Jiangsu Province, Grant Number: BK20140365.

CONFLICT OF INTEREST STATEMENT

The authors declare no conflict of interest.

ORCID

Ziye Chen  <http://orcid.org/0000-0001-6865-4869>

Lingyun Wang  <http://orcid.org/0000-0002-9380-6032>

REFERENCES

- Wang F, Wang M, She Z, Fan K, Xu C, Chu B, et al. Collagen/chitosan based two-compartment and bi-functional dermal scaffolds for skin regeneration. *Mater Sci Eng C*. 2015;52:155–62.
- Abdelrahman I, Steinvall I, Sjöberg F, Ellabban MA, Zdolsek J, Elmasry M. Pros and cons of early and late skin grafting in children with burns—evaluation of common concepts. *Eur Burn J*. 2022;37(1):180–7.
- van Zuijlen PP, Van Trier AJ, Vloemans JF, Groenevelt F, Kreis RW, Middelkoop E. Graft survival and effectiveness of dermal substitution in burns and reconstructive surgery in a one-stage grafting model. *Plastic Reconstruct Surgery*. 2000;106(3): 615–23.
- Janik S, Eljazzar R, Faisal M, Grasl S, Vyskocil E, Miles BA, et al. Outcome in patients with partial and full-thickness cheek defects following free flap reconstruction—a multicentric analysis of 47 cases. *J Clin Med*. 2020;9(6):1740.
- Hallock GG. The utility of both muscle and fascia flaps in severe upper extremity trauma. *J Trauma Acute Care Surgery*. 2002;53(1):61–5.
- Shimizu R, Kishi K. Skin graft. *Plastic Surgery Int*. 2012; 2012:563493.
- Petkar KS, Dhanraj P, Kingsly PM, Sreekar H, Lakshmanarao A, Lamba S, et al. A prospective randomized controlled trial comparing negative pressure dressing and conventional dressing methods on split-thickness skin grafts in burned patients. *Burns*. 2011;37(6):925–9.
- Sun BK, Siprashvili Z, Khavari PA. Advances in skin grafting and treatment of cutaneous wounds. *Science*. 2014;346(6212):941–5.
- Mirzaei-parsa MJ, Ghanbari H, Alipoor B, Tavakoli A, Najafabadi MRH, Faridi-Majidi R. Nanofiber-acellular dermal matrix as a bilayer scaffold containing mesenchymal stem cell for healing of full-thickness skin wounds. *Cell Tissue Res*. 2019;375(3):709–21.
- Niimi Y, Baba K, Tsuchida M, Takeda A. A histological evaluation of artificial dermal scaffold used in micrograft treatment: a case study of micrograft and NPWT performed on a postoperative ulcer formation after tumor resection. *Medicina*. 2022;58(1):73.
- Parcells AL, Karcich J, Granick MS, Marano MA. The use of fetal bovine dermal scaffold (PriMatrix) in the management of full-thickness hand burns. *Eplasty*. 2014;14:e36.
- Sharma V, Kohli N, Moulding D, Afolabi H, Hook L, Mason C, et al. Design of a novel two-component hybrid dermal scaffold for the treatment of pressure sores. *Macromol Biosci*. 2017;17(11):1700185.
- Hodde J. Naturally occurring scaffolds for soft tissue repair and regeneration. *Tissue Eng*. 2002;8(2):295–308.
- Mazlyzam AL, Aminuddin BS, Fuzina NH, Norhayati MM, Fauziah O, Isa MR, et al. Reconstruction of living bilayer human skin equivalent utilizing human fibrin as a scaffold. *Burns*. 2007;33(3):355–63. <https://www.sciencedirect.com/science/article/pii/S0305417906002506>
- Zhou H, You C, Wang X, Jin R, Wu P, Li Q, et al. The progress and challenges for dermal regeneration in tissue engineering. *J Biomed Mater Res A*. 2017;105(4):1208–18.
- Tavelli L, Barootchi S, Di Gianfilippo R, Modarressi M, Cairo F, Rasperini G, et al. Acellular dermal matrix and coronally advanced flap or tunnel technique in the treatment of multiple adjacent gingival recessions. A 12-year follow-up from a randomized clinical trial. *J Clin Periodontol*. 2019;46(9):937–48.
- Xu Z, Chen X, Tan R, She Z, Chen Z, Xia Z. Preparation and characterization of a gallium-loaded antimicrobial artificial dermal scaffold. *Mater Sci Eng C*. 2019;105:110063.
- Zhang Q, Chen S, You R, Tariq Z, Huang J, Li M, et al. Silk fibroin/hyaluronic acid porous scaffold for dermal wound healing. *Fibers Polymers*. 2017;18(6):1056–63.
- Heimbach DM, Warden GD, Luterman A, Jordan MH, Ozobia N, Ryan CM, et al. Multicenter postapproval clinical

- trial of integra[®] dermal regeneration template for burn treatment. *J Burn Care Rehab.* 2003;24(1):42–8.
20. Rnjak-Kovacina J, Wise SG, Li Z, Maitz PK, Young CJ, Wang Y, et al. Electrospun synthetic human elastin: collagen composite scaffolds for dermal tissue engineering. *Acta Biomater.* 2012;8(10):3714–22.
 21. Chandika P, Ko SC, Oh GW, Heo SY, Nguyen VT, Jeon YJ, et al. Fish collagen/alginate/chitosan oligosaccharides integrated scaffold for skin tissue regeneration application. *Int J Biol Macromol.* 2015;81:504–13.
 22. Vahidi M, Frounchi M, Dadbin S. Porous gelatin/poly (ethylene glycol) scaffolds for skin cells. *Soft Mater.* 2017;15(1):95–102.
 23. Asran AS, Razghandi K, Aggarwal N, Michler GH, Groth T. Nanofibers from blends of polyvinyl alcohol and polyhydroxy butyrate as potential scaffold material for tissue engineering of skin. *Biomacromolecules.* 2010;11(12):3413–21.
 24. Bonvallet PP, Culpepper BK, Bain JL, Schultz MJ, Thomas SJ, Bellis SL. Microporous dermal-like electrospun scaffolds promote accelerated skin regeneration. *Tissue Eng Part A.* 2014;20(17–18):2434–45.
 25. Matsumoto Y, Ikeda K, Yamaya Y, Yamashita K, Saito T, Hoshino Y, et al. The usefulness of the collagen and elastin sponge derived from salmon as an artificial dermis and scaffold for tissue engineering. *Biomed Res.* 2011;32(1):29–36.
 26. Li J, Ren N, Qiu J, Jiang H, Zhao H, Wang G, et al. Carbodiimide crosslinked collagen from porcine dermal matrix for high-strength tissue engineering scaffold. *Int J Biol Macromol.* 2013;61:69–74.
 27. Brown SJ, Surti F, Sibbons P, Hook L. Wound healing properties of a fibrin-based dermal replacement scaffold. *Biomed Phys Eng Express.* 2021;8(1):015025.
 28. Huang S, Deng T, Wang Y, Deng Z, He L, Liu S, et al. Multifunctional implantable particles for skin tissue regeneration: preparation, characterization, in vitro and in vivo studies. *Acta Biomater.* 2008;4(4):1057–66.
 29. Sung HJ, Meredith C, Johnson C, Galis ZS. The effect of scaffold degradation rate on three-dimensional cell growth and angiogenesis. *Biomaterials.* 2004;25(26):5735–42.
 30. Zomer HD, da Silva Jeremias T, Ratner B, Trentin AG. Mesenchymal stromal cells from dermal and adipose tissues induce macrophage polarization to a pro-repair phenotype and improve skin wound healing. *Cytherapy.* 2020;22(5):247–60.
 31. Sharma V, Patel N, Kohli N, Ravindran N, Hook L, Mason C, et al. Viscoelastic, physical, and bio-degradable properties of dermal scaffolds and related cell behaviour. *Biomed Mater.* 2016;11(5):055001.
 32. Chawla R, Tan A, Ahmed M, Crowley C, Moimen NS, Cui Z, et al. A polyhedral oligomeric silsesquioxane-based bilayered dermal scaffold seeded with adipose tissue-derived stem cells: in vitro assessment of biomechanical properties. *J Surgical Res.* 2014;188(2):361–72.
 33. Agostinis C, Spazzapan M, Vuerich R, Balduit A, Stocco C, Mangogna A, et al. Differential capability of clinically employed dermal regeneration scaffolds to support vascularization for tissue bioengineering. *Biomedicine.* 2021;9(10):1458.
 34. Yan S, Zhang Q, Wang J, Liu Y, Lu S, Li M, et al. Silk fibroin/chondroitin sulfate/hyaluronic acid ternary scaffolds for dermal tissue reconstruction. *Acta Biomaterialia.* 2013;9(6):6771–82.
 35. Ojeh N, Frame J, Navsaria H. In vitro characterization of an artificial dermal scaffold. *Tissue Eng.* 2001;7(4):457–72.
 36. Kuhn C, Angehrn F. Use of high-resolution ultrasound to monitor the healing of leg ulcers: a prospective single-center study. *Skin Res Technol.* 2009;15(2):161–7.
 37. Ghetia M, Bondioli E, Purpura V, Cenacchi G, Ruscelli P, Melandri D. Decellularized human dermal matrix produced by a skin bank. *Ann Ital Chir.* 2017;88(5):443–8.
 38. Wang Z, Pan H, Yuan Z, Liu J, Chen W, Pan Y. Assessment of dermal wound repair after collagen implantation with optical coherence tomography. *Tissue Eng C: Methods.* 2008;14(1):35–45.
 39. Fox K, Tran PA, Lau DW, Ohshima T, Greentree AD, Gibson BC. Nanodiamond-polycaprolactone composite: a new material for tissue engineering with sub-dermal imaging capabilities. *Mater Lett.* 2016;185:185–8.
 40. Huang D, Swanson Eric A, Lin Charles P, Schuman Joel S, Stinson William G, Chang W, et al. Optical coherence tomography. *Science.* 1991;254(5035):1178–81.
 41. Carrasco-Zevallos OM, Viehland C, Keller B, Draelos M, Kuo AN, Toth CA, et al. Review of intraoperative optical coherence tomography: technology and applications [Invited]. *Biomed Optics Express.* 2017;8(3):1607–37.
 42. Hagag AM, Gao SS, Jia Y, Huang D. Optical coherence tomography angiography: technical principles and clinical applications in ophthalmology. *Taiwan J Ophthalmol.* 2017;7(3):115–29.
 43. Everett M, Magazzeni S, Schmoll T, Kempe M. Optical coherence tomography: from technology to applications in ophthalmology. *Transl Biophoton.* 2021;3(1):e202000012.
 44. Gambichler T, Pljakic A, Schmitz L. Recent advances in clinical application of optical coherence tomography of human skin. *Clin Cosmet Investig Dermatol.* 2015;8:345–54.
 45. Ulrich M, Themstrup L, de Carvalho N, Manfredi M, Grana C, Ciardo S, et al. Dynamic optical coherence tomography in dermatology. *Dermatology.* 2016;232(3):298–311.
 46. Jonas O, Jon H, Gregor BEJ. Advances in optical coherence tomography in dermatology—a review. *J Biomed Optics.* 2018;23(4):040901. <https://doi.org/10.1117/1.JBO.23.4.040901>
 47. Sattler EC, Köstle R, Welzel J. Optical coherence tomography in dermatology. *J Biomed Optics.* 2013;18(6):061224.
 48. Ferrante di Ruffano L, Dinnes J, Deeks JJ, Chuchu N, Bayliss SE, Davenport C, et al. Optical coherence tomography for diagnosing skin cancer in adults. *Cochrane Database System Rev.* 2018;12:CD013189.
 49. Coleman AJ, Richardson TJ, Orchard G, Uddin A, Choi MJ, Lacy KE. Histological correlates of optical coherence tomography in non-melanoma skin cancer. *Skin Res Technol.* 2013;19(1):e10–19.
 50. Wan B, Ganier C, Du-Harpur X, Harun N, Watt F, Patalay R, et al. Applications and future directions for optical coherence tomography in dermatology. *British J Dermatol.* 2021;184(6):1014–22.
 51. Cobb MJ, Chen Y, Underwood RA, Usui ML, Olerud J, Li X. Noninvasive assessment of cutaneous wound healing using ultrahigh-resolution optical coherence tomography. *J Biomed Optics.* 2006;11(6):064002.
 52. Alvin TY, Bunsho K, Woong Gyu J, Zhongping C, John Stuart Nelson MD, Bruce JT. Imaging wound healing using optical coherence tomography and multiphoton microscopy in an *in vitro* skin-equivalent tissue model. *J Biomed Optics.* 2004;9(2):248–53.
 53. Deegan AJ, Wang W, Men S, Li Y, Song S, Xu J, et al. Optical coherence tomography angiography monitors human cutaneous wound healing over time. *Quantitat Imaging Med Surgery.* 2018;8(2):135–50.
 54. Maier T, Sattler E, Braun-Falco M, Ruzicka T, Berking C. High-definition optical coherence tomography for the in vivo detection of demodex mites. *Dermatology.* 2012;225(3):271–6.
 55. Spöler F, Först M, Marquardt Y, Hoeller D, Kurz H, Merk H, et al. High-resolution optical coherence tomography as a non-destructive monitoring tool for the engineering of skin equivalents. *Skin Res Technol.* 2006;12(4):261–7.
 56. Marx U, Pickert D, Heymer A, Schmitt R. Non-invasive quality control for production processes of artificial skin equivalents by optical coherence tomography. *Proc CIRP.* 2013;5:128–32.

57. Sanchez MM, Orneles DN, Park BH, Morgan JT. Automated epidermal thickness quantification of in vitro human skin equivalents using optical coherence tomography. *BioTechniques*. 2022;72(5):194–200.
58. Qiu X, Wang J, Wang G, Wen H. Vascularization of Lando® dermal scaffold in an acute full-thickness skin-defect porcine model. *J Plastic Surgery Hand Surgery*. 2018;52(4):204–9.
59. Kugelman J, Alonso-Caneiro D, Read SA, Hamwood J, Vincent SJ, Chen FK, et al. Automatic choroidal segmentation in OCT images using supervised deep learning methods. *Sci Reports*. 2019;9(1):13298.
60. Dos Santos VA, Schmetterer L, Stegmann H, Pfister M, Messner A, Schmidinger G, et al. CorneaNet: fast segmentation of cornea OCT scans of healthy and keratoconic eyes using deep learning. *Biomed Optics Express*. 2019;10(2):622–41.
61. Ronneberger O, Fischer P, Brox T. U-Net: convolutional networks for biomedical image segmentation, Springer International Publishing; 2015.
62. Zhou Z, Siddiquee M, Tajbakhsh N, Liang J. UNet++: redesigning skip connections to exploit multiscale features in image segmentation. *IEEE Trans Med Imaging*. 2020;39(6):1856–67.
63. Oktay O, Schlemper J, Folgoc LL, Lee M, Heinrich M, Misawa K, et al. Attention U-Net: learning where to look for the pancreas. *arXiv preprint*. 2018. Available from: <http://arxiv.org/abs/1804.03999>
64. Mou L, Zhao Y, Chen L, Cheng J, Liu J. CS-Net: channel and spatial attention network for curvilinear structure segmentation. In: *Medical Image Computing and Computer Assisted Intervention—MICCAI 2019, 22nd International Conference, Shenzhen, China, October 13–17, 2019, Proceedings, Part I*; 2019.
65. Yang C, Zhou X, Zhu W, Xiang D, Chen Z, Yuan J, et al. Multi-discriminator adversarial convolutional network for nerve fiber segmentation in confocal corneal microscopy images. *IEEE J Biomed Health Inform*. 2021;26:648–59. <https://go.exlibris.link/ZHPsGvKg>
66. Wang W, Yu Y, Jiang Y, Qu J, Niu L, Yang J, et al. Silk fibroin scaffolds loaded with angiogenic genes in adenovirus vectors for tissue regeneration. *J Tissue Eng Regenerat Med*. 2019;13(5): 715–28.

How to cite this article: Chen Z, Cheng Q, Wang L, Mo Y, Li K, Mo J. Optical coherence tomography for in vivo longitudinal monitoring of artificial dermal scaffold. *Lasers Surg Med*. 2023;1–11. <https://doi.org/10.1002/lsm.23645>